nature materials

Article

https://doi.org/10.1038/s41563-026-02624-4

Strain-insensitive wet-tissue-adhesive biphasic bioelectronics for physicochemical monitoring and adaptive therapy

Received: 25 June 2025

Accepted: 6 May 2026

Published online: 10 June 2026

Check for updates

Jiahong Li, Kexin Fan, Xiaotian Ma, Canran Wang, Jihong Min, Yonglin Chen, Yu Song, Yadong Xu & Wei Gao

Implantable bioelectronics are rapidly advancing towards multifunctional platforms capable of real-time monitoring and therapeutic intervention. However, designing implants with stable, long-term integration with soft, dynamic biological tissues, especially under strain or movement, is still challenging. Here we introduce a stretchable, strain-insensitive, wet-tissue-adhesive elastomer–hydrogel biphasic platform for cross-functional bioelectronics, enabling simultaneous physical sensing, chemical monitoring and neural modulation in vivo. This platform, termed ElHyX, features a molecularly integrated elastomer–hydrogel architecture, functionalized with conductive fillers to achieve mechanical compliance, robust electrical performance and strong tissue adhesion without the need for sutures or additional surface treatments. Using direct ink writing, we fabricated customizable ElHyX-based devices for in vivo electrocardiogram monitoring, glucose sensing and nerve stimulation. A closed-loop system for diabetic management in rats was also developed, where real-time biosignal detection autonomously triggered neuromodulation to regulate blood glucose levels. Overall, our findings establish ElHyX as a versatile, scalable platform for next-generation bioelectronics, capable of continuous physicochemical monitoring and autonomous therapeutic intervention in complex biological environments.

Implantable bioelectronics have become critical tools in modern medicine, enabling continuous physiological monitoring, precise diagnostics and targeted therapeutic interventions[1–3]. Despite considerable advancements, current implants remain constrained by rigid form factors, mechanical mismatch with soft biological tissues, and limited functionality—often confined to electrical sensing or stimulation. These shortcomings can compromise signal fidelity, provoke adverse tissue responses and ultimately result in premature device failure, especially in dynamic environments such as the beating heart or expanding gastrointestinal tract[4].

To address these challenges, recent efforts have explored flexible and stretchable systems based on structural engineering[5,6], stretchable polymer composites[7,8] and conductive hydrogels[9–11]. While these approaches enhance mechanical compatibility, they each face trade-offs: engineered structures often reduce device density, polymer composites may lose conductivity under strain[12–14], and hydrogels—although inherently soft—typically exhibit low conductivity (<0.5 S cm^{-1}) and present challenges in electronic system integration and durability[15–17].

Hybrid solutions combining conductive materials with hydrogel have demonstrated improved tissue compatibility and adhesion[18–22]. However, these approaches often involve complex fabrication procedures, post-fabrication processing or additional surgical steps.

Andrew and Peggy Cherng Department of Medical Engineering, Division of Engineering and Applied Science, California Institute of Technology, Pasadena, CA, USA. e-mail: weigao@caltech.edu

These complexities hinder scalability, limit spatial control over the device–tissue interface and pose challenges for clinical translation. Many existing platforms still rely on sutures or surgical adhesives and fall short of offering a scalable, unified solution that supports both sensing and therapeutic functionalities.

A particularly underdeveloped area in implantable electronics is chemical sensing, which holds immense potential to enrich the functional scope of bioelectronic implants. Unlike electrical signals that reflect neuronal or muscular activity, chemical biomarkers offer more direct insights into dynamic physiological states at molecular levels[23–25]. Local biochemical changes in specific organs or interstitial fluids—such as those associated with inflammation, metabolic dysregulation or ischaemia—often precede systemic symptoms and are not easily captured through conventional electrical modalities[26,27]. Seamlessly incorporating real-time chemical sensing into soft, tissue-conforming bioelectronic systems therefore represents a critical step towards multimodal, adaptive implants capable of richer physiological interrogation and closed-loop intervention.

In this work, we present, ElHyX, a soft, strain-insensitive elastomer–hydrogel biphasic cross-functional platform for implantable bioelectronics. ElHyX enables multimodal functionalities—including physical sensing, biochemical monitoring and neural modulation—by integrating a conductive elastomer matrix with a tissue-adhesive hydrogel layer (Fig. 1a and Supplementary Fig. 1). Functional fillers such as eutectic gallium–indium (EGaIn) and graphite impart robust electrical and electrochemical performance, while the hydrogel component ensures conformal adhesion to dynamic, wet tissue surfaces without additional treatment. In contrast to conventional flexible devices (Fig. 1b) that require sutures and exhibit poor conformability to soft moving organs, ElHyX maintains stable performance under physiological deformation while gently interfacing with soft organs.

This biphasic platform enables fabrication of diverse device types—including bioelectrical sensors, biochemical sensors and nerve cuffs—all of which can be readily adapted to conform and adhere to various internal organs for physiological sensing and metabolic regulation (Fig. 1c). Importantly, this platform is compatible with scalable manufacturing via direct ink writing (DIW) (Fig. 1d, Supplementary Fig. 2 and Supplementary Video 1), enabled by a custom-developed set of printable inks optimized for both rheological printability and functional performance (Supplementary Fig. 3 and Supplementary Table 1). The molecularly integrated elastomer–hydrogel interface provides robust mechanical compliance, strong wet-tissue adhesion and reliable operation under dynamic strain (Fig. 1e and Supplementary Video 2).

We demonstrate the versatility of ElHyX across a series of in vivo applications, including electrocardiogram (ECG) monitoring on a beating heart, real-time glucose sensing and neural modulation (Fig. 1c). Furthermore, we integrate these functions seamlessly into a single platform (Fig. 1f) to realize a closed-loop system for automated blood glucose regulation in a diabetic animal model. Compared with the state-of-the-art implantable bioelectronic platforms, ElHyX uniquely combines high stretchability, strain-invariant conductivity, wet-tissue adhesion, multimodal sensing and therapeutic actuation—positioning it as a comprehensive and scalable solution for next-generation implantable bioelectronics[7,11,28–32] (Fig. 1g and Supplementary Tables 2 and 3).

Mechanical and electromechanical characterizations of ElHyX

ElHyX is a biphasic platform that integrates conductive elastomers with a bioadhesive hydrogel, offering seamless molecular integration, tunable conductivity and rapid strong adhesion to wet tissue surfaces for implantable bioelectronics. The architecture comprises a hydrogel phase covalently bonded to an elastomer composite, with EGaIn confined to the central elastomeric domain (Fig. 2a). Cross-sectional scanning electron microscopy (SEM) imaging confirms this biphasic architecture, showing uniform hydrogel–elastomer integration and spatially localized EGaIn distribution (Fig. 2b).

Poly(styrene-butadiene-styrene) (SBS) was chosen as the elastomer backbone owing to its excellent stretchability and mechanical durability. To enable seamless two-phase integration at molecular level, SBS was chemically modified to introduce vinyl side chains, producing acrylyl-opening epoxidized SBS (AESBS) via sequential epoxidation and acrylation (Fig. 2c). Fourier-transform infrared (FTIR) spectra confirm successful functionalization, with characteristic peaks observed for SBS, epoxidized SBS (ESBS) and AESBS (Fig. 2d). These vinyl groups serve as active sites for radical polymerization, allowing molecular level integration between hydrogel and elastomer without the need for additional surface treatments. This integration strategy allows the elastomer and hydrogel phases to form a chemically independent yet mechanically seamless interface (Supplementary Fig. 4), supporting robust adhesion and mechanical integrity while allowing independent optimization of elastomer properties through functional fillers and hydrogel formulation flexibility.

The hydrogel phase is built on a poly(acrylic acid) (PAAc) backbone that achieves stable wet-tissue adhesion through a high density of strong hydrogen bonding between carboxylic acid groups and biological surfaces[33,34]. To enhance mechanical robustness, we introduced sodium 4-vinylbenzenesulfonate and [2-(acryloyloxy)ethyl]trimethylammonium via copolymerization, to generate ionic crosslinks and form an ionically crosslinked hydrogel (i-Gel). These dynamic bonds can enhance energy dissipation and improve hydrogel toughness[35]. Following polymerization, a dry adhesive layer (DAL) is formed by dehydrating the hydrogel, enabling rapid rehydration and adhesion to moist tissue through water absorption and hydrogen bonding.

Leveraging this hydrogel design, ElHyX exhibits strong and stable adhesion to wet biological tissues (Fig. 2e). The incorporation of dynamic ionic crosslinks facilitates reversible bond exchange and enhanced energy dissipation during deformation, enhancing the hydrogel's mechanical integrity and preserving cohesive strength even after swelling[36]. By contrast, hydrogels lacking ionic crosslinking became compromised upon swelling, leading to rapid mechanical failure (Fig. 2f). This cohesive resilience is critical for maintaining reliable wet-tissue adhesion, as interfacial bonding can exceed the internal strength of swollen hydrogels. ElHyX incorporating ionically crosslinked i-Gel maintains robust adhesion across multiple tissue types after swelling, whereas versions lacking ionic reinforcement delaminate or disintegrate quickly (Fig. 2g,h). In addition, ElHyX-based bioelectronics can be detached from tissue on demand by applying a high concentration urea solution, which weakens the hydrogen bonds between i-Gel and tissue (Supplementary Video 3). This reversible adhesion mechanism provides a safe pathway for device retrieval. Owing to its high formulation flexibility, the ElHyX platform could also be extended towards biodegradable or bioresorbable designs using bioresorbable polymer, degradable hydrogels and transient metals, enabling temporary implantation scenarios with controlled functional lifetimes[22,37–41].

EGaIn was selected as the conductive filler for the elastomer phase owing to its liquid nature, which ensures electrical continuity under deformation. When embedded within an SBS elastomer matrix, EGaIn remains confined, preventing leakage while preserving the composite's low modulus and high stretchability (Fig. 2i and Supplementary Figs. 5–7). Initially non-conductive due to oxide shells surrounding EGaIn particles, the composite becomes conductive through mechanical activation—such as compression or stretching—that ruptures the shells and forms conductive pathways. In practice, the minor deformation that occurs naturally during peeling of the printed device from the substrate is sufficient to rupture the oxide shells surrounding the embedded EGaIn particles, thereby forming continuous conductive pathways (Supplementary Video 4). SEM imaging after stretching confirms the formation of continuous conductive

https://doi.org/10.1038/s41563-026-02624-4

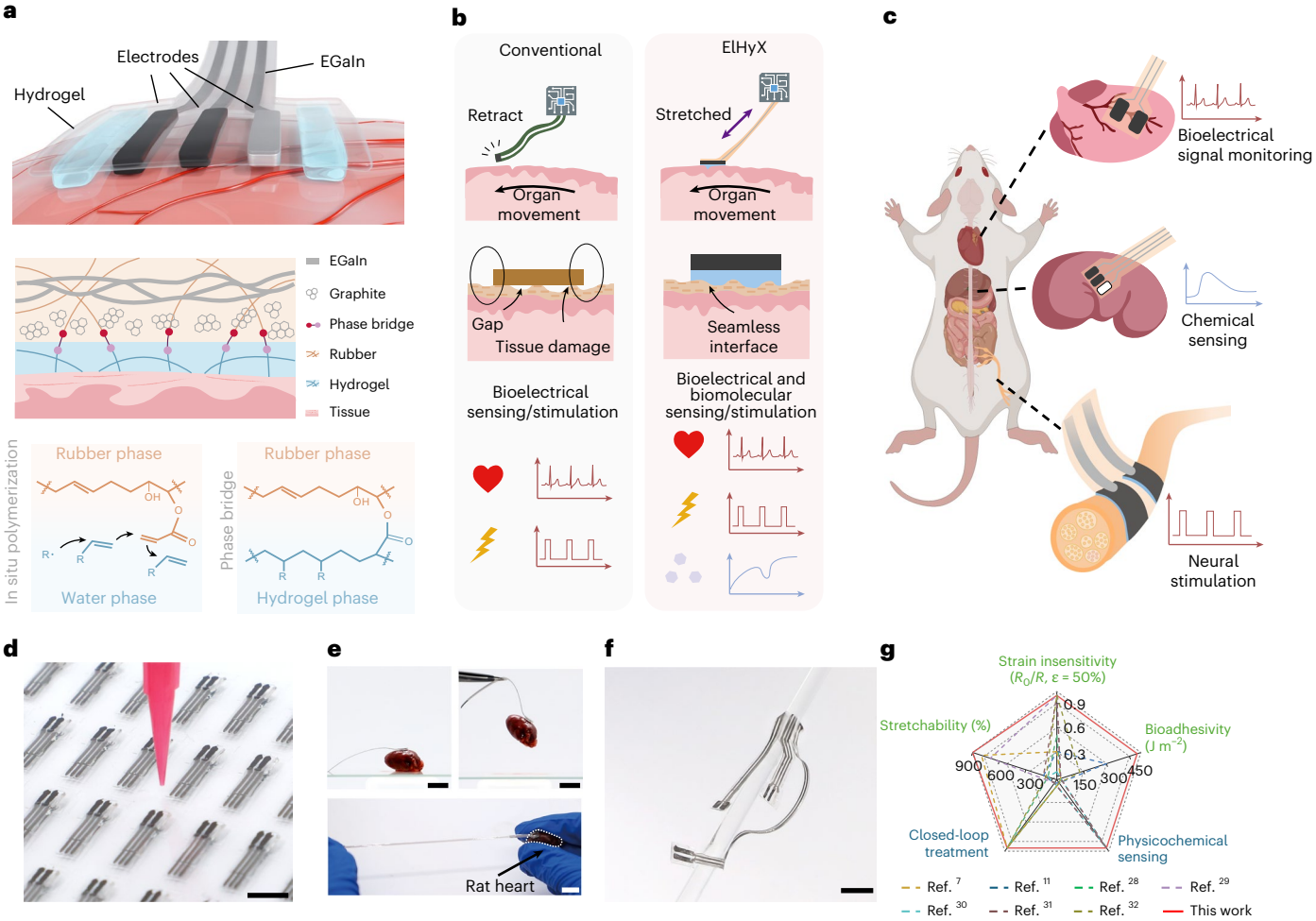

Fig. 1 | Overview of the strain-insensitive elastomer–hydrogel biphasic multifunctional platform (ElHyX) for multimodal implantable bioelectronics. **a**, Schematic illustration of the ElHyX architecture. The elastomer phase is chemically modified with vinyl groups that participate in hydrogel polymerization, enabling seamless molecular-level integration. Conductive fillers such as EGaIn and graphite provide strain-insensitive conductivity and an electrochemically stable interface. A bioadhesive hydrogel ensures robust adhesion to wet tissue. **b**, Compared with conventional flexible electrodes, ElHyX eliminates the needs for sutures and enables secure, conformal integration onto soft, dynamic organs while supporting biomolecular sensing. **c**, Schematic of ElHyX implants applied to various organs for multimodal physiological monitoring and modulation. **d**, The ElHyX system can be manufactured rapidly at scale using DIW. Scale bar, 1 cm. **e**, Demonstrations of ElHyX adhesion and functional stability under large deformation (100% strain) and on an isolated rat heart. Scale bars, 1 cm. **f**, Photo of an integrated ElHyX device combining electrophysiological sensing, biomolecular monitoring and neural modulation for closed-loop disease management. Scale bar, 1 cm. **g**, Radar chart benchmarking ElHyX against other state-of-the-art implantable bioelectronic platforms across key materials and functionality metrics. The ElHyX system uniquely combines high stretchability, strain-insensitive performance, wet-tissue adhesion, multimodal physicochemical sensing and therapeutic feedback capabilities.

networks via particle coalescence (Fig. 2j). Electrical measurements reveal a sharp conductivity increase from insulating to ~4×10^3 S m^{-1} after a 10% strain stretching cycle, and up to ~1×10^5 S m^{-1} after a 500% strain stretching cycle (Supplementary Fig. 8). Benefiting from the fluidic reconfigurability of EGaIn (Fig. 2k), the EGaIn-SBS composite maintains stable conductivity with minimal resistance change (~15%) even under 900% strain, and shows negligible hysteresis during cyclic loading. By contrast, conventional conductive elastomers that rely on solid conductive fillers experience major conductivity loss upon mechanical deformation (Fig. 2l,m). Moreover, the EGaIn-SBS system exhibits excellent durability and reliability, with no substantial resistance drift after 1,000 cycles of 200% stretching (Fig. 2n).

Strain-insensitive bioelectrical and biomolecular sensors

Graphite was selected as the conductive filler for both bioelectrical and biomolecular sensing electrodes owing to its excellent electrochemical stability. For the bioelectrical sensor, the bioadhesive hydrogel is directly polymerized onto the graphite-AESBS electrode, enabling a seamless tissue–device interface and stable signal acquisition. By contrast, biomolecular sensors feature hydrogel polymerized on AESBS substrate adjacent to the electrodes, preserving open diffusion paths for analytes and ensuring unobstructed molecular transport (Fig. 3a).

To enable enzymatic biomolecular sensing, Prussian blue (PB) is incorporated into the graphite-SBS composite to create graphite-PB-SBS electrodes capable of detecting hydrogen peroxide (H_2O_2)—a common by-product in enzymatic reactions—at a low operation potential (0.0 V versus Ag/AgCl), thereby minimizing the interferences from other electroactive species. PB is uniformly blended into the ink formulation (Supplementary Fig. 9) and printed via DIW for reproducible electrode fabrication. Additional functional fillers such as polyaniline (PANI)—which exhibits high sensitivity and reversible electrochemical behaviour—and carbon nanotubes (CNTs)—which provide superior electrical conductivity and strong electrocatalytic activity towards uric acid—were integrated to achieve high-performance pH

https://doi.org/10.1038/s41563-026-02624-4

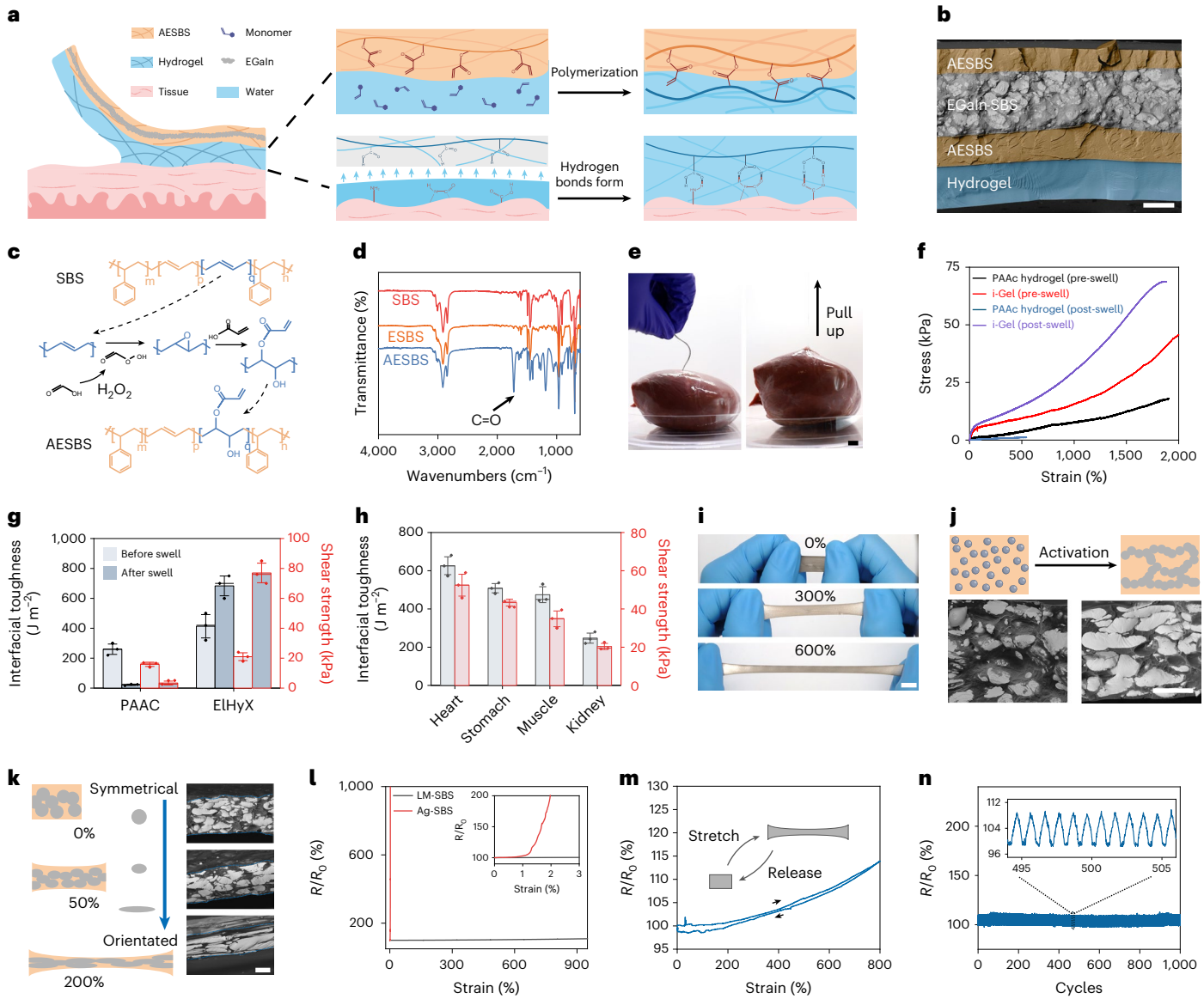

Fig. 2 | Mechanical and electromechanical characterizations of ElHyX. **a**, Schematic of ElHyX formation via in situ hydrogel polymerization on a chemically modified elastomer. Water is removed from the hydrogel to form a DAL that rapidly absorbs interfacial moisture and forms hydrogen bonds with tissue. **b**, Cross-sectional SEM image of ElHyX, showing seamless integration between elastomer, conductive filler and hydrogel. Scale bar, 100 µm. **c**, Synthesis process of AESBS through epoxidation and acrylation of SBS. **d**, FTIR spectra of SBS, ESBS and AESBS. **e**, Photograph of ElHyX conformally adhered to a porcine heart. Scale bar, 1 cm. **f**, Stress–strain curves of hydrogels with and without ionic crosslinking. **g**, Comparison of adhesion performances of hydrogels with and without ionic crosslinks before and after swelling on porcine skin. Error bars represent the s.d. of the mean from three samples. **h**, Tissue adhesion strength of the DAL on various biological tissues. Error bars represent the s.d. of the mean from three samples. **i**, Photographs of EGaIn-SBS under 0%, 300% and 600% strain. Scale bar, 1 cm. **j**, Schematic and SEM images of EGaIn-SBS showing particle coalescence and activation of EGaIn-SBS after mechanical deformation. Scale bar, 50 µm. **k**, Schematic and cross-section SEM images of EGaIn-SBS under 0%, 50% and 200% strain. Scale bar, 50 µm. **l**, Relative resistance changes (R/R_0) of EGaIn-SBS compared with silver-SBS composites under uniaxial strain. Inset, zoomed in to low-strain range. **m**, Relative resistance hysteresis of EGaIn-SBS over an 800% stretch–release cycle. **n**, Relative resistance changes of EGaIn-SBS over 1,000 cycles at 200% strain.

and uric acid sensing, respectively. These functionalities were further validated in vivo (Supplementary Figs. 10 and 11).

Cross-sectional SEM imaging of the printed electrode confirms the uniform dispersion of fillers within the elastomer phase and their cohesive integration with the bioadhesive hydrogel (Fig. 3b). The DIW process enables precise spatial patterning of all functional composites (Fig. 3c and Supplementary Figs. 12 and 13), and the graphite-PB-SBS electrode exhibits a roughened surface morphology that enhances electrochemical sensitivity (Supplementary Fig. 14).

Owing to the seamless tissue–hydrogel interface, the ElHyX-based bioelectrical sensor exhibits substantially lower impedance compared to dry electrodes and performs on par with commercial gel electrodes (3M Red Dot) of the same size (Fig. 3d). Robust wet-tissue adhesion and strain-insensitive signal acquisition are demonstrated in ECG and electromyography (EMG) recordings, which remains stable under 100% tensile strain (Fig. 3e,f and Supplementary Fig. 15). By contrast, electrodes based solely on conventional solid conductive fillers often suffer from cracking or conductivity loss under large deformation (Supplementary Fig. 16). We further demonstrated the advantages of ElHyX's bioadhesive and stretchable properties by mounting an ElHyX-based light-emitting diode (LED) array onto an isolated porcine heart (Fig. 3g and Supplementary Video 5). The device functioned

https://doi.org/10.1038/s41563-026-02624-4

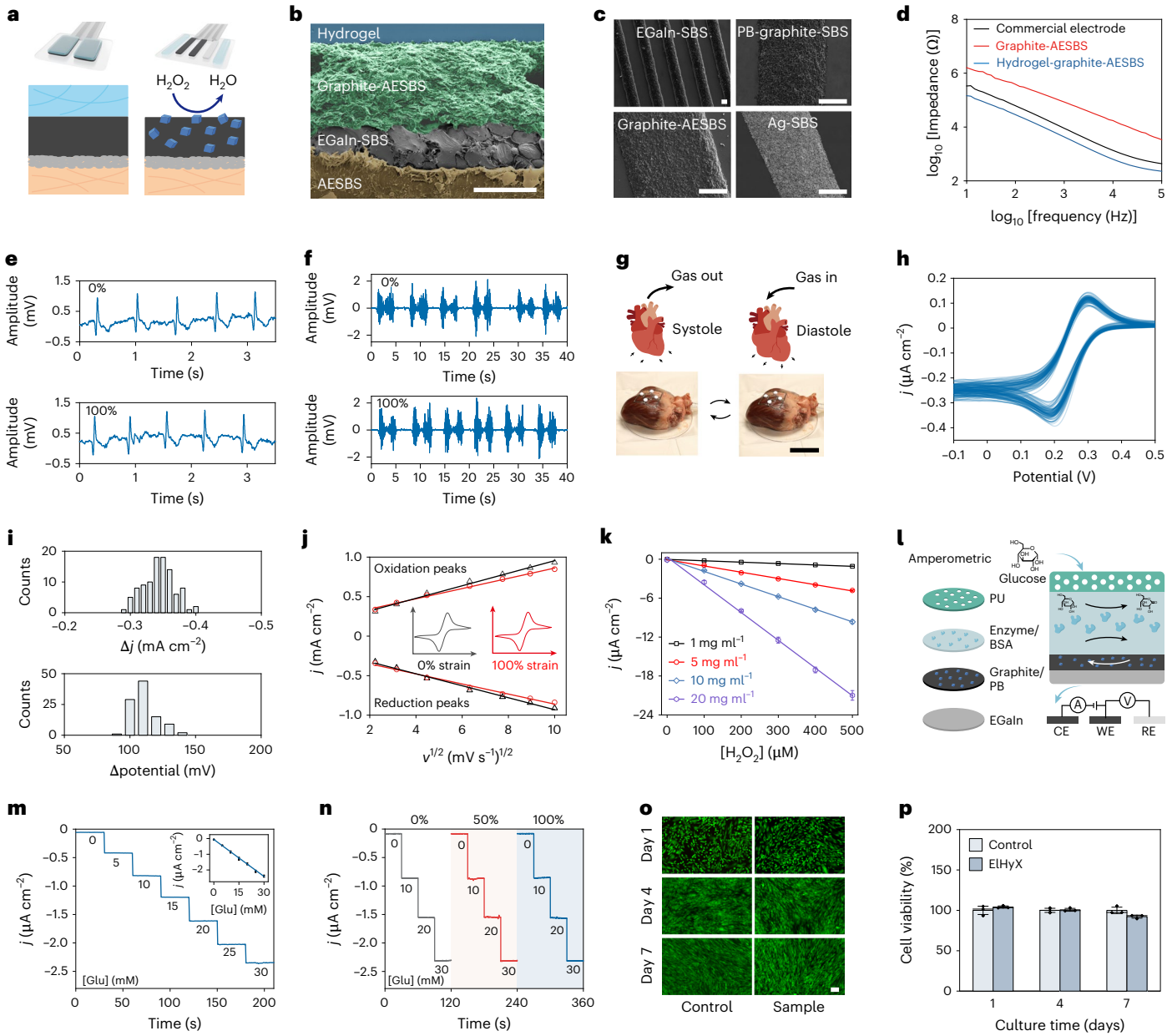

Fig. 3 | Characterization of strain-insensitive ElHyX physical and chemical sensors. a, Schematic of ElHyX biophysical and biochemical sensors. **b**, Cross-sectional SEM image of ElHyX ECG electrode structure. Scale bar, 100 µm. **c**, SEM image of printed elastomer composites used in sensor fabrication. Scale bars, 100 µm. **d**, Skin–electrode impedance comparison of graphite-AESBS electrodes with and without hydrogel, and commercial gel electrodes. **e**,**f**, ElHyX bioelectrical sensor under 0% and 100% strain for ECG (**e**) and EMG (**f**) recording on human participants. **g**, In vitro demonstration of ElHyX-based LED array functioning on a beating porcine heart. Scale bar, 5 cm. **h**,**i**, Cyclic voltammograms (CVs) of 100 graphite-PB-SBS electrodes in 5 mM $K_3Fe(CN)_6$ (**h**) and statistic distribution of reduction peak current density and redox peak potential difference (**i**). **j**, Current peak densities of CVs of graphite-PB-SBS electrodes in 5 mM $K_3Fe(CN)_6$ under 0% (black) and 100% (red) strain, plotted against the square root of scan rates ($v^{1/2}$). **k**, Amperometric calibration of graphite-PB electrodes with varying PB loadings in for H_2O_2 detection. Error bars represent the s.d. of the mean from three sensors. **l**, Schematic of enzymatic glucose sensor immobilized on graphite-PB-SBS electrodes and overlaid with a PU diffusion-limiting layer. CE, counter electrode; WE, working electrode; RE, reference electrode. **m**, Amperometric calibration of ElHyX-based glucose sensors. Error bars represent the s.d. of the mean from three sensors. Inset: linear calibration curve showing the relationship between the current response and glucose concentration. **n**, Strain-insensitive glucose detection under 0%, 50% and 100% strain. **o**, Representative live (green)/dead (red) images of HDFs seeded with and without ElHyX electrodes after 1-day, 4-day and 7-day culture. Scale bar, 100 µm. **p**, Quantitative analysis of metabolic activity over a 7-day culture period. Error bars represent the s.d. of the mean from three samples.

reliably with no signs of delamination during artificial heartbeats, indicating that ElHyX can maintain stable performance on dynamically moving organs.

Electrochemical characterization using the Fe^{3+}/Fe^{2+} redox system demonstrated excellent reproducibility (Fig. 3h,i and Supplementary Fig. 17) and stable performance under 100% strain (Fig. 3j and Supplementary Fig. 18), underscoring the strain-insensitive nature of the ElHyX electrochemical sensors. Sensor sensitivity to H_2O_2 was tunable by adjusting PB concentration in the graphite-PB-SBS electrode (Fig. 3k). A glucose-sensing electrode was fabricated by printing an enzyme layer—comprising glucose oxidase and bovine serum albumin (BSA)—followed by a polyurethane (PU) diffusion-limiting layer onto the

https://doi.org/10.1038/s41563-026-02624-4

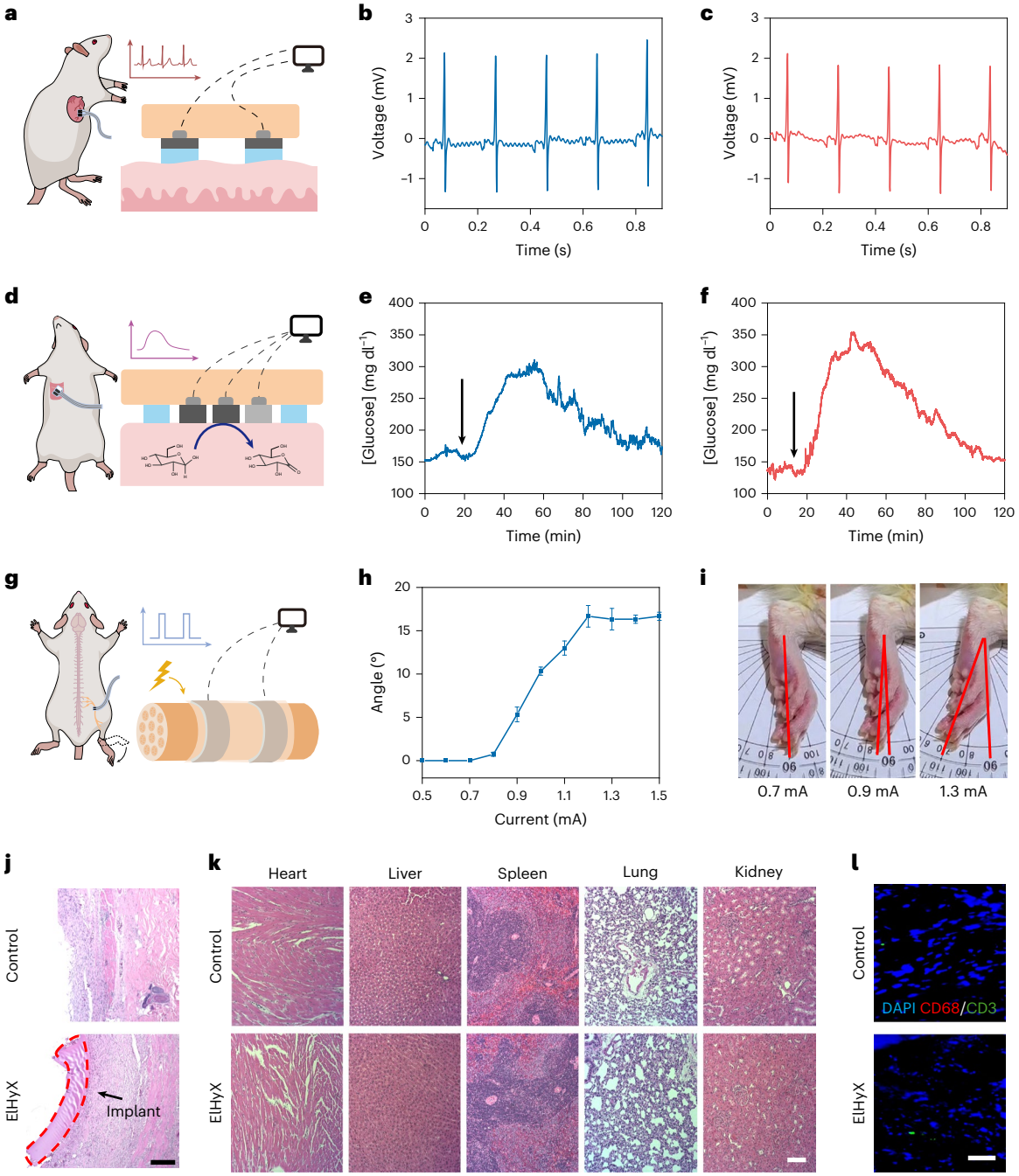

Fig. 4 | In vivo characterization of ElHyX-based implantable electronics. **a**, Schematic illustrating the implantation of ElHyX-based ECG sensor on the surface of a rat heart. **b**,**c**, Representative ECG waveforms recorded at 0 h and 24 h post-implantation. **d**, Schematic of an ElHyX glucose sensor implanted on the outer surface of the rib cage of a rat to detect interstitial glucose. **e**,**f**, Real-time glucose monitoring using ElHyX electrode immediately after implantation (**e**) and 24 h after implantation (**f**). A glucose dose (0.36 g kg^{-1}) was administered via retro-orbital injection at the time indicated by the arrow. **g**, Schematic of ElHyX electrode wrapping around the sciatic nerve for electrical stimulation and motor response. **h**, Quantitative analysis of leg flexion angles in response to different electrical stimulation currents, showing a dose-dependent motor response. Error bars represent the s.d. of the mean from three trials. **i**, Photographs of rat hindlimb flexion under stimulation currents of 0.7 mA, 0.9 mA and 1.3 mA, respectively. **j**,**k**, Histological evaluation of surrounding tissues (**j**) and main organs (**k**) via H&E staining after 28 days of implantation. Scale bars, 100 µm. **l**, Immunofluorescence staining of inflammatory markers in tissue surrounding the implant at day 28. Green, red and blue represent lymphocyte (CD3), macrophages (CD68) and cell nuclei, respectively. Scale bar, 50 µm.

graphite-PB-SBS electrode (Fig. 3l), achieving high sensitivity, linearity, selectivity and stability at physiologically relevant glucose concentrations (Fig. 3m and Supplementary Fig. 19). In addition, the sensor maintains consistent performance under mechanical deformation, confirming its strain-insensitive properties (Fig. 3n and Supplementary Fig. 20).

Finally, in vitro biocompatibility was confirmed using live/dead staining and PrestoBlue metabolic assays with human dermal fibroblasts (HDF) (Fig. 3o,p). High cell viability and metabolic activity over 7 days validate the cytocompatibility of ElHyX for in vivo applications.

https://doi.org/10.1038/s41563-026-02624-4

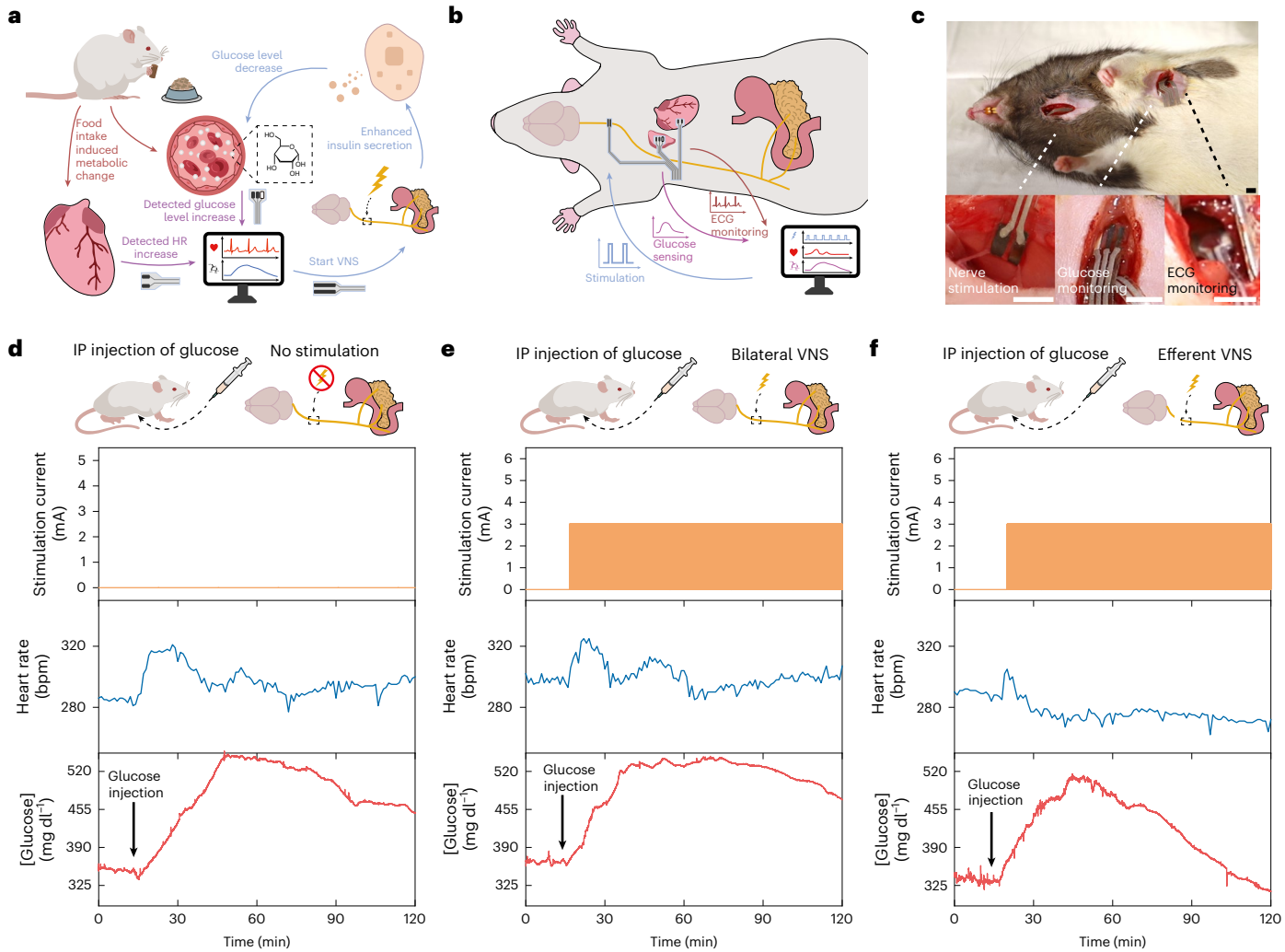

Fig. 5 | In vivo evaluation of ElHyX-based closed-loop blood glucose regulation in diabetic rats. a, Schematic of the closed-loop blood glucose management concept: food intake triggers increases in blood glucose and heart rate (HR), which are sensed in real time and used to initiate VNS for insulin modulation. **b**,**c**, Schematic (**b**) and photograph (**c**) of the multifunctional ElHyX device implanted in a diabetic rat, showing the ECG sensor attached to the heart, the glucose sensor on the outer rib surface, and nerve cuff wrapped around the vagus nerve. Scale bars, 5 mm. **d**, In vivo monitoring of blood glucose levels and heart rate following IP glucose injection without VNS. **e**, In vivo evaluation of blood glucose levels and heart rate following IP glucose injection with bilateral VNS. **f**, In vivo demonstration of closed-loop blood glucose management after IP glucose injection with selective eVNS.

In vivo evaluation of ElHyX for physicochemical sensing and neural stimulation

We evaluated the ElHyX platform in vivo to demonstrate its multifunctional capabilities, including electrophysiological monitoring, biochemical sensing and neural stimulation (Supplementary Fig. 21). For electrophysiological monitoring, ElHyX electrodes were placed directly onto the surface of a rat heart to acquire ECG signals. The ionically conductive hydrogel enabled immediate and robust adhesion to the beating myocardium, forming a conformal, low-impedance interface between the conductive graphite and wet tissue (Fig. 4a and Supplementary Video 6). This seamless integration facilitated efficient transmission of biopotentials, yielding high-fidelity ECG recordings (Fig. 4b). Importantly, the signal quality remained stable after 24 h of implantation (Fig. 4c), highlighting the hydrogel's strong and durable adhesion in dynamic physiological environments.

To demonstrate the platform's real-time chemical sensing capability, glucose was selected as a representative biomarker. The ElHyX sensor was implanted onto the rib cage of a rat, targeting interstitial fluid diffusion from surrounding tissues to simulate deep organ biochemical monitoring sites such as the liver, kidney or gastrointestinal tract (Fig. 4d and Supplementary Fig. 22). Following retro-orbital injection of glucose (0.36 g kg^{-1}), the sensor detected a rapid and quantifiable increase in glucose levels, followed by a gradual decline to baseline as glucose was metabolized (Fig. 4e). A repeated measurement 24 h after implantation produced a comparable response, confirming the device's stability and functional longevity in vivo (Fig. 4f). To further evaluate the in vivo stability and dynamic performance of physiological signal monitoring, we conducted continuous recordings for 6 h (Supplementary Fig. 23) and multiple glucose elevation and clearance cycles (Supplementary Fig. 24). The results confirm the excellent stability, responsiveness and signal fidelity of ElHyX-based sensors during prolonged physiological monitoring in vivo.

To improve long-term stability, we incorporated an additional PU encapsulation layer printed around the original ElHyX structure (Supplementary Fig. 25a–c). Devices were implanted in rats and evaluated on day 14 post-implantation through glucose sensing, ECG recording and sciatic nerve stimulation. Clear signal recordings and consistent stimulation efficiency were observed (Supplementary Fig. 25d,e), demonstrating that the elastomer–hydrogel integration preserved strong tissue adhesion, electrical continuity and mechanical integrity

over time. These results establish the long-term robustness and biofunctional reliability of the ElHyX platform under physiologically dynamic conditions.

To assess ElHyX for bioelectronic therapy, we used it as a neural stimulation interface. A soft, flexible ElHyX electrode strip was wrapped around the rat sciatic nerve without sutures to form a conformal, suture-free nerve cuff (Fig. 4g and Supplementary Fig. 21). The sciatic nerve was successfully activated, eliciting observable hindlimb movements. We quantified the stimulation–response relationship by delivering graded current amplitudes through the ElHyX nerve cuff. The degree of leg flexion increased with stimulation intensity, ultimately reaching a saturation point at higher currents (Fig. 4h,i and Supplementary Video 7), demonstrating effective and tunable neural modulation.

Finally, in vivo systemic biocompatibility of ElHyX was assessed through histological analysis. Haematoxylin and eosin (H&E) staining of the surrounding tissues and major organs—including the heart, liver, spleen, lungs and kidneys—revealed no observable pathological abnormalities or inflammation (Fig. 4j,k and Supplementary Fig. 26a,b). In addition, immunofluorescence staining and quantitative analysis of subcutaneously implanted ElHyX samples showed minimal presence of leukocytes (CD3, green) and macrophages (CD68, red) at 28 days post-implantation (Fig. 4l and Supplementary Fig. 26c), confirming the biosafety and long-term biocompatibility of ElHyX for chronic implantable applications.

Closed-loop blood glucose regulation in diabetic rats

To demonstrate the therapeutic potential of ElHyX, we established a closed-loop system for diabetes management integrating real-time sensing and neuromodulation (Fig. 5a). Following food intake, both heart rate and blood glucose levels increase. These physiological changes are concurrently monitored by implanted ElHyX sensors—an electrochemical glucose sensor and an ECG sensor. Once elevated glucose and heart rate levels are detected, targeted vagus nerve stimulation (VNS) is triggered to promote insulin secretion and facilitate glucose clearance[42].

To validate this concept, we fabricated a multifunctional implantable device based on ElHyX that supports simultaneous ECG recording, glucose monitoring and VNS (Fig. 5b). The device was surgically implanted into diabetic rats, with individual modules positioned for optimal function: the ECG electrode on the heart, the glucose sensor on the rib cage, and the nerve cuff around the vagus nerve (Fig. 5c and Supplementary Fig. 21). This system can also be configured into a compact and wireless format for long-term, multimodal physiological monitoring and closed-loop regulation (Supplementary Figs. 27–29).

Hyperglycaemia was induced via intraperitoneal (IP) glucose injection (2 g kg^{-1}), which led to concurrent elevations in heart rate and blood glucose levels, peaking ~30 min after injection (~550 mg dl^{-1}). A control injection of saline elicited no notable physiological changes (Supplementary Fig. 30), confirming the specificity of the glucose-induced response. In untreated diabetic rats, glucose levels remained elevated for an extended period (Fig. 5d). We subsequently applied bilateral VNS in response to the elevated glucose and heart rate, as defined by our dual-parameter closed-loop logic (Supplementary Fig. 31). However, despite stimulation (5 Hz, 3 mA, 0.5 ms pulse width), blood glucose levels remained elevated for an extended period (Fig. 5e). This inefficacy is probably due to the simultaneous activation of afferent and efferent vagal fibres, as afferent VNS has been shown to stimulate hepatic glucose release and suppress insulin secretion[43]. The stimulation parameters used in our study were selected on the basis of previous reports of effective VNS for metabolic modulation in rodent models[44]. To further evaluate their physiological effects, we performed in vivo optimization experiments in healthy rats while monitoring heart rate under different stimulation conditions. Heart rate decreased progressively with increasing stimulation current and reached a plateau once the current exceeded the effective threshold (Supplementary Fig. 32a). Within the low-frequency range (1–5 Hz), stimulation produced comparable effects on heart rate (Supplementary Fig. 32b). To circumvent this limitation, we implemented selective efferent VNS (eVNS) for targeted stimulation. This strategy minimizes off-target activation of afferent fibres and associated side effects, enabling more specific modulation of metabolic pathways. Following detection of elevated physiological markers, eVNS was applied using the same stimulation parameters. In contrast to bilateral VNS, eVNS notably attenuated the glucose peak (~515 mg dl^{-1}) and accelerated glucose normalization, returning to baseline within 90 min (Fig. 5f). To further assess system-level reliability, multicycle closed-loop glucose regulation experiments were conducted over 3 consecutive days and up to 1 month in vivo (Supplementary Fig. 33). Consistent feedback-triggered glucose regulation and repeatable performance across sessions confirmed the stability and reproducibility of the ElHyX-based closed-loop system during extended operation. These results demonstrate sustained closed-loop neuromodulation and support the potential of ElHyX-enabled automatic, responsive regulation of metabolic disorders under long-term physiological conditions.

Outlook

With its modular and tunable design, ElHyX can be readily adapted for a broad spectrum of biomarkers and therapeutic targets, enabling next-generation bioelectronic interfaces that integrate multimodal sensing, adaptive actuation and autonomous feedback control. By enabling the stable co-integration of chemical biosensing, electrophysiological recording and neuromodulation within a single soft, bioadhesive and fully printed platform, this materials–systems strategy allows device functionality to be reconfigured through formulation-level tuning rather than structural redesign. This capability facilitates rapid adaptation across diverse sensing and therapeutic modalities while maintaining mechanical compliance, electrochemical stability and scalable manufacturing. Looking forward, such platform-level integration may accelerate the development of implantable bioelectronic systems for long-term physiological monitoring and closed-loop therapeutic intervention in complex biological environments.

Online content

Any methods, additional references, Nature Portfolio reporting summaries, source data, extended data, supplementary information, acknowledgements, peer review information; details of author contributions and competing interests; and statements of data and code availability are available at https://doi.org/10.1038/s41563-026-02624-4.

References

1. Al-Khatib, S. M. Cardiac implantable electronic devices. *N. Engl. J. Med.* **390**, 442–454 (2024).
2. Krauss, J. K. et al. Technology of deep brain stimulation: current status and future directions. *Nat. Rev. Mater.* **17**, 75–87 (2021).
3. Carlson, M. L. Cochlear implantation in adults. *N. Engl. J. Med.* **382**, 1531–1542 (2020).
4. Barrese, J. C. et al. Failure mode analysis of silicon-based intracortical microelectrode arrays in non-human primates. *J. Neural Eng.* **10**, 066014 (2013).
5. Park, S. I. et al. Soft, stretchable, fully implantable miniaturized optoelectronic systems for wireless optogenetics. *Nat. Biotechnol.* **33**, 1280–1286 (2015).
6. Jin, P. et al. A flexible, stretchable system for simultaneous acoustic energy transfer and communication. *Sci. Adv.* **7**, eabg2507 (2021).
7. Choi, S. et al. Highly conductive, stretchable and biocompatible Ag–Au core–sheath nanowire composite for wearable and implantable bioelectronics. *Nat. Nanotechnol.* **13**, 1048–1056 (2018).

8. Zhong, D. et al. High-speed and large-scale intrinsically stretchable integrated circuits. *Nature* **627**, 313–320 (2024).
9. Liu, Y. et al. Soft and elastic hydrogel-based microelectronics for localized low-voltage neuromodulation. *Nat. Biomed. Eng.* **3**, 58–68 (2019).
10. Tringides, C. M. et al. Viscoelastic surface electrode arrays to interface with viscoelastic tissues. *Nat. Nanotechnol.* **16**, 1019–1029 (2021).
11. Zhou, T. et al. 3D printable high-performance conducting polymer hydrogel for all-hydrogel bioelectronic interfaces. *Nat. Mater.* **22**, 895–902 (2023).
12. Sempionatto, J. R. et al. An epidermal patch for the simultaneous monitoring of haemodynamic and metabolic biomarkers. *Nat. Biomed. Eng.* **5**, 737–748 (2021).
13. Zhou, W. et al. Gas-permeable, ultrathin, stretchable epidermal electronics with porous electrodes. *ACS Nano* **14**, 5798–5805 (2020).
14. Stoyanov, H., Kollosche, M., Risse, S., Waché, R. & Kofod, G. Soft conductive elastomer materials for stretchable electronics and voltage controlled artificial muscles. *Adv. Mater.* **25**, 578–583 (2013).
15. Wei, H. et al. Orthogonal photochemistry-assisted printing of 3D tough and stretchable conductive hydrogels. *Nat. Commun.* **12**, 2082 (2021).
16. Naficy, S., Oveissi, F., Patrick, B., Schindeler, A. & Dehghani, F. Printed, flexible pH sensor hydrogels for wet environments. *Adv. Mater. Technol.* **3**, 1800137 (2018).
17. Pan, L. et al. An ultra-sensitive resistive pressure sensor based on hollow-sphere microstructure induced elasticity in conducting polymer film. *Nat. Commun.* **5**, 3002 (2014).
18. Shin, Y. et al. Low-impedance tissue-device interface using homogeneously conductive hydrogels chemically bonded to stretchable bioelectronics. *Sci. Adv.* **10**, eadi7724 (2024).
19. Lim, C. et al. Highly conductive and stretchable hydrogel nanocomposite using whiskered gold nanosheets for soft bioelectronics. *Adv. Mater.* **36**, 2407931 (2024).
20. Li, N. et al. Bioadhesive polymer semiconductors and transistors for intimate biointerfaces. *Science* **381**, 686–693 (2023).
21. Li, J. et al. Tough adhesives for diverse wet surfaces. *Science* **357**, 378–381 (2017).
22. Yang, Q. et al. Photocurable bioresorbable adhesives as functional interfaces between flexible bioelectronic devices and soft biological tissues. *Nat. Mater.* **20**, 1559–1570 (2021).
23. Sempionatto, J. R., Lasalde-Ramírez, J. A., Mahato, K., Wang, J. & Gao, W. Wearable chemical sensors for biomarker discovery in the omics era. *Nat. Rev. Chem.* **6**, 899–915 (2022).
24. Yang, Y. & Gao, W. Wearable and flexible electronics for continuous molecular monitoring. *Chem. Soc. Rev.* **48**, 1465–1491 (2019).
25. Ronkainen, N. J., Halsall, H. B. & Heineman, W. R. Electrochemical biosensors. *Chem. Soc. Rev.* **39**, 1747–1763 (2010).
26. Martin, W. R. W., Wieler, M. & Gee, M. Midbrain iron content in early Parkinson disease. *Neurology* **70**, 1411–1417 (2008).
27. Serkova, N., Klawitter, J. & Niemann, C. U. Organ-specific response to inhibition of mitochondrial metabolism by cyclosporine in the rat. *Transpl. Int.* **16**, 748–755 (2003).
28. Sunwoo, S.-H. et al. Ventricular tachyarrhythmia treatment and prevention by subthreshold stimulation with stretchable epicardial multichannel electrode array. *Sci. Adv.* **9**, eadf6856 (2023).
29. Xu, Y. et al. Phase-separated porous nanocomposite with ultralow percolation threshold for wireless bioelectronics. *Nat. Nanotechnol.* **19**, 1158–1167 (2024).
30. Li, R. et al. A flexible and physically transient electrochemical sensor for real-time wireless nitric oxide monitoring. *Nat. Commun.* **11**, 3207 (2020).
31. Zhao, Y. et al. Soft strain-insensitive bioelectronics featuring brittle materials. *Science* **378**, 1222–1227 (2022).
32. Lee, S. et al. A shape-morphing cortex-adhesive sensor for closed-loop transcranial ultrasound neurostimulation. *Nat. Electron.* **7**, 800–814 (2024).
33. Nie, B., Stutzman, J. & Xie, A. A vibrational spectral maker for probing the hydrogen-bonding status of protonated Asp and Glu residues. *Biophys. J.* **88**, 2833–2847 (2005).
34. Chen, J. et al. An adhesive hydrogel with "load-sharing" effect as tissue bandages for drug and cell delivery. *Adv. Mater.* **32**, 2001628 (2020).
35. Rao, P. et al. Tough hydrogels with fast, strong, and reversible underwater adhesion based on a multiscale design. *Adv. Mater.* **30**, 1801884 (2018).
36. Sun, T. L. et al. Physical hydrogels composed of polyampholytes demonstrate high toughness and viscoelasticity. *Nat. Mater.* **12**, 932–937 (2013).
37. Freedman, B. R. et al. Degradable and removable tough adhesive hydrogels. *Adv. Mater.* **33**, 2008553 (2021).
38. Choi, Y. S. et al. A transient, closed-loop network of wireless, body-integrated devices for autonomous electrotherapy. *Science* **376**, 1006–1012 (2022).
39. Khan, A. et al. Highly elastic, biodegradable polyester-based citrate rubber for 3D printing in regenerative engineering. *ACS Biomater. Sci. Eng.* **11**, 1571–1582 (2025).
40. Guo, J. et al. Recent advances in gelatin methacryloyl hydrogels for bone regeneration. *ACS Appl. Nano Mater.* **7**, 17193–17213 (2024).
41. Kang, S.-K., Koo, J., Lee, Y. K. & Rogers, J. A. Advanced materials and devices for bioresorbable electronics. *Acc. Chem. Res.* **51**, 988–998 (2018).
42. Kawana, Y. et al. Optogenetic stimulation of vagal nerves for enhanced glucose-stimulated insulin secretion and β cell proliferation. *Nat. Biomed. Eng.* **8**, 808–822 (2024).
43. Meyers, E. E., Kronemberger, A., Lira, V., Rahmouni, K. & Stauss, H. M. Contrasting effects of afferent and efferent vagal nerve stimulation on insulin secretion and blood glucose regulation. *Physiol. Rep.* **4**, e12718 (2016).
44. Yin, J., Ji, F., Gharibani, P. & Chen, J. D. Z. Vagal nerve stimulation for glycemic control in a rodent model of type 2 diabetes. *Obes. Surg.* **29**, 2869–2877 (2019).

Publisher's note Springer Nature remains neutral with regard to jurisdictional claims in published maps and institutional affiliations.

Springer Nature or its licensor (e.g. a society or other partner) holds exclusive rights to this article under a publishing agreement with the author(s) or other rightsholder(s); author self-archiving of the accepted manuscript version of this article is solely governed by the terms of such publishing agreement and applicable law.

© The Author(s), under exclusive licence to Springer Nature Limited 2026

Methods

All animal procedures were approved by the Institutional Animal Care and Use Committee at the California Institute of Technology.

Materials and reagents

SBS, PANI, acrylic acid, hydroquinone, sodium 4-vinylbenzenesulfonate, [2-(acryloyloxy)ethyl]trimethylammonium chloride solution (80 wt%), poly(ethylene glycol) diacrylate-575 (PEGDA-575), sodium chloride (NaCl), hydrogen peroxide (H_2O_2) (30% (w/v)), potassium ferricyanide (III) ($K_3Fe(CN)_6$), uric acid, BSA, glucose oxidase, glutaraldehyde (50 wt%) and PU were purchased from Sigma-Aldrich. Silver flake, graphite flake, EGaIn, poly(ethylene glycol)-600 (PEG-600, iron (III) chloride ($FeCl_3$), tetrahydrofuran and L-lactic acid were purchased from Thermo Fisher Scientific. Toluene, methanol, ascorbic acid, dextrose (D-glucose), phosphate-buffered saline (PBS) solution and potassium chloride were purchased from Fisher Scientific. PB, formic acid and Butvar B-98 were purchased from Acros Organics. Multiwalled CNTs was purchased from Beijing Boyu. 2-Oxoglutaric acid was purchased from Tokyo Chemical Industry. Polydimethylsiloxane (PDMS) (SYLGARD 184) was purchased from Dow Corning. Poly(vinyl alcohol) (molecular weight 125,000 Da, 88% hydrolysed) was purchased from Polysciences.

Preparation of customizable inks

SBS ink (25 wt%) was prepared by dissolving SBS in toluene under magnetic stirring. To formulate graphite-SBS, graphite-PANI-SBS, CNTs-SBS, Ag-SBS and EGaIn-SBS, a specified amount of the respective fillers was homogeneously mixed into the SBS ink using a planetary centrifugal mixer (THINKY, AR-100) for 5 min. To develop graphite-PB-SBS ink for the preparation of working and counter electrode for chemical sensors, PB powder was dispersed in toluene by probe sonication, followed by dissolving SBS (25 wt%) into the suspension. The resulted PB-SBS ink was then mixed with graphite through planetary centrifugal mixer for 5 min (Supplementary Fig. 7).

To synthesize AESBS, SBS was first epoxidized according to the method described in the literature[45]. In brief, 5 g SBS, 560 µl formic acid and 50 µl PEG-600 were dissolved in 50 ml toluene with magnetic stir under 60 °C. Then, 1.5 ml H_2O_2 was dropped into the solution. The reaction was conducted at 60 °C for 2 h, followed by precipitating and washing with methanol. The solid was dried under nitrogen flow overnight to give ESBS. To introduce vinyl side chains, ESBS was then acrylated according to the method in literature[46]. In brief, 3.5 g ESBS, 19 ml acrylic acid and 17 mg hydroquinone was dissolved in 35 ml toluene under magnetic stirring. The reaction was conducted at 60 °C for 24 h, followed by precipitating and washing with methanol. The product was dried under nitrogen flow overnight to give AESBS.

AESBS ink (25 wt%) was prepared by dissolving AESBS in toluene by magnetic stirring. To formulate graphite-AESBS, 20 wt% graphite was homogeneously mixed into AESBS ink using planetary centrifugal mixer. To prepare glucose oxidase enzyme cocktail ink, glucose oxidase (0.1 mg ml^{-1}) and bovine serum albumin (0.1 g ml^{-1}) were dissolved in PBS. To further stabilize the enzyme, the resulting solution was mixed with glutaraldehyde solution (1 wt%) at a volume ratio of 20:1. To prepare the diffusion-limiting membrane ink, PU (50 mg ml^{-1}) was dissolved in tetrahydrofuran under magnetic stirring. To prepare the ink for the reference membrane that stabilizes the reference electrode, Butvar (78 mg ml^{-1}) and NaCl (50 mg ml^{-1}) were dissolved in methanol, followed by vigorous agitation in an ultrasonic bath for 30 min. To prepare the adhesive hydrogel ink, 1.5 ml acrylic acid, 0.3 ml [2-(acryloyloxy)ethyl]trimethylammonium chloride solution (80 wt%), 250 mg sodium 4-vinylbenzenesulfonate, 0.2 ml PEGDA-575 solution (1.25 wt%) and 0.6 ml 2-oxogluaric acid solution (3.6 wt%) were mixed with 2.15 ml poly(vinyl alcohol) solution (10 wt%) via magnetic stirring in a dark environment.

Fabrication of ElHyX-based bioelectronics

The ElHyX-based bioelectronics were fabricated through an all-printed process on PDMS-coated glass slides (Supplementary Fig. 2). This involved the serial printing of multiple layers, including substrate (SBS/AESBS), interconnects (EGaIn-SBS), electrical sensing/stimulation electrodes (graphite-AESBS), electrochemical working/counter electrodes (graphite-PB-SBS, graphite-PANI-SBS or CNTs-SBS), reference electrodes (Ag-SBS), encapsulation (SBS) and adhesive hydrogel using a three-axis robotic deposition stage (Aerotech). The printing paths were defined by G-code. The customized inks were loaded into 15-ml syringe barrels equipped with tapered tips ranging from 150 µm to 250 µm in diameter. The extrusion of ink was controlled by applying high pressure air through a benchtop fluid dispenser (EFD Nordson). The patch was then exposed to 360-nm ultraviolet light under nitrogen protection for 15 min to polymerize the hydrogel, followed by overnight drying under nitrogen flow to remove residual water from the hydrogel.

To prepare the glucose sensor, glucose oxidase enzyme cocktail was printed on the electrochemical working electrode (graphite-PB-SBS) and air-dried overnight under 4 °C. A PU diffusion-limiting layer was subsequently printed onto the resulting electrode. To further stabilize the reference electrode, the Ag-SBS electrode was treated with 0.1 M $FeCl_3$ solution to form a surface AgCl layer. A reference membrane cocktail was then printed onto the electrode and air-dried overnight at room temperature (22 °C).

Rheology characterization

Rheological characterizations of the customized inks were conducted using a rheometer (Anton Paar, MCR 302) equipped with a parallel-plate measuring system with a 25 mm diameter. The tests were conducted with a 1 mm gap size.

Morphology characterization

The surface and cross-section structures of the printed ElHyX platform were studied by optical microscopy (ZEISS) and SEM (ZEISS 1550VP Field Emission SEM). Before SEM imaging, a ~10-nm layer of platinum was sputtered onto the sample surface. SEM imaging was performed at an acceleration voltage of 15 kV.

Mechanical characterization

Testing samples were printed into a rectangular shape with length/width of 20 mm/5 mm. Tensile and loading–unloading tests were performed using a motorized force tester (Mark-10) at a deformation rate of 10 mm min^{-1} in air at room temperature. Cyclic stretching tests for fatigue were performed at a deformation rate of 100 mm min^{-1}.

For adhesion tests, all porcine tissues were purchased from local markets and were recovered to room temperature (22 °C) before use. The tissues and adhesive platforms were fixed to a polyethylene terephthalate substrate using medical tape before testing. Adhesive platforms were adhered to the tissue surface by gently pressing at ~5 kPa for 1 min.

The interfacial toughness was tested by 180° peel test (ATSM F2256) using a motorized force tester (Mark-10) at a deformation rate of 50 mm min^{-1}. The shear strength was tested by lap-shear test (ATSM F2255) with a mechanical test machine (Mark-10) at a deformation rate of 50 mm min^{-1}.

On-body biopotential signal recording

ElHyX-based electrical sensing electrodes were used to record electrophysiological signals. For ECG and EMG monitoring, the skin at the electrode placement site was prewetted with saline. For ECG monitoring, electrodes were positioned on the right and left arms (Supplementary Fig. 15), and the device was mechanically fixed to maintain the prescribed tensile strain during recording. For EMG monitoring, electrodes were placed at both ends of the biceps brachii muscle. Electrophysiological signals were captured using a PowerLab data acquisition system (ADInstruments) and processed through a 50-Hz

low-pass filter in LabChart software. For impedance measurement, the ElHyX electrodes were attached to human forearm in a two-electrode configuration with a frequency range of 10 Hz to 100 kHz under ambient conditions. Measurements were performed using an electrochemical workstation (CH Instruments). All study participants provided written informed consent before their involvement in the research.

Electrochemical characterization of biochemical sensors

In vitro electrochemical analyses were conducted using CHI840D and CHI760 (CH Instruments) electrochemical workstations under ambient temperature. CV was used to assess the performance of the graphite-PB-SBS electrodes. For in vitro H_2O_2 and glucose sensing characterization, amperometric measurements were conducted at a potential of 0 V in PBS (pH 7.4).

Electronic system design and characterization

An electronic system was integrated into a two-layer flexible printed circuit board designed using Eagle CAD. The energy of the system was harnessed from a 3.7 V lithium battery. A voltage regulator (catalogue no. ADP162; Analog Devices) was used to manage the power of the system, ensuring reliable and stable power delivery. ECG measurement is achieved by a heart rate monitor front end (catalogue no. AD8232; Analog Devices). Wireless communication and control were implemented using a radio frequency module (catalogue no. nRF52832; Nordic), which enabled wireless data transmission, signal processing and operation of the electrochemical instrumentation system based on the AD5940 (Analog Devices). The electronic system supports continuous operation with an average power consumption of 0.52 mW during Bluetooth Low Energy communication and 67 mW during full operation, including sensing, electrical stimulation and wireless data transmission via Bluetooth Low Energy (Supplementary Fig. 28). Power consumption was measured using a power profiler (catalogue no. PPK2; Nordic Semiconductor). The electronic components, including the circuit board and battery, were fully encapsulated with PDMS to prevent direct contact between tissues and electronic materials and to ensure electrical insulation and biocompatibility during implantation.

In vitro biocompatibility

HDFs and the complete HDF cell culture media were acquired from ATCC. The incubator for cell culture was set at 37 °C and 5% CO_2. The tested samples were ~3 mm × 3 mm in dimension, and were disinfected by washing with 70% ethanol and exposing them to ultraviolet light for 30 min. HDFs were first rejuvenated in a T25 flask before seeding to the 24-well microplate. In total, 5×10^4 cells were seeded in each well on day 0. Then, 0.6 ml of cell culture media was added to each well, with a 0.1 ml addition to the transwell (Corning Costar). The sterilized samples were placed into the transwells.

The cell viability was tested on days 1, 4 and 7. PrestoBlue (Thermo Fisher Scientific) mixed with the culture media (10%:90%, v/v) was added to each well at a volume of 0.3 ml after the removal of the transwells. After 45 min of co-culture with HDF cells in the incubator, 0.1 ml of the solution was transferred to a 96-well microplate for plate reading (540 nm excitation/590 nm emission, BioTek Instruments).

On day 7, after the PrestoBlue cell viability test, live/dead cell imaging and viability tests were conducted using the LIVE/DEADTM Viability/Cytotoxicity Kit (Invitrogen). For cell staining, 0.5 µl ml^{-1} of calcein AM and 2 µl ml^{-1} of ethidium homodimer-1 in Dulbecco's PBS (DPBS) were added to each well, followed by incubation in the incubator for 45 min. Live cells were labelled green, while dead cells were labelled red. After washing the cells twice with DPBS, the stained cells were imaged using an Axio Observer inverted microscope (ZEISS). The green image was captured using the fluorescein isothiocyanate (FITC) filter, while the red image was captured using the cyanine-3 (Cy3) filter. The images were overlaid using ImageJ software.

In vivo evaluation of ElHyX-based bioelectronics

The animal studies in this work were performed in accordance with the protocol approved by Caltech Institutional Animal Care and Use Committee (protocol nos. IA23-1800, IA23-1870 and IA23-1872). Experiments were performed in 12-week-old male healthy rats (Sprague-Dawley, Charles River Laboratories) and 12-week-old male diabetic rats (ZDF obese fa/fa, Charles River Laboratories).

To evaluate the performance of ElHyX-based ECG sensors, healthy rats were connected to a mechanical ventilator (RoVent, KentScientific) and were anaesthetized and administered analgesia using 1.5–2.5% (v/v) isoflurane, ketoprofen (5 mg kg^{-1}), Ethiqa XR (3.25 mg kg^{-1}) and bupivacaine (1 mg kg^{-1}), and a 1-cm incision between the third and fourth ribs was made to expose the thoracic cavity. Then, the ElHyX-based ECG sensor was adhered to the heart surface. The incision was closed with 5–0 Prolene (for rib cage and muscles) and 4–0 Nylon (for skin) sutures. The animals were ventilated with 100% oxygen until autonomous breathing was regained. On day 0 and day 1 after implantation, the animals were anaesthetized using 1.5–2.5% (v/v) isoflurane. The output end of the implanted ElHyX-based ECG sensor was connected to PowerLab for signal recording.

To evaluate the performance of ElHyX-based glucose sensors, healthy rats were anaesthetized and administered analgesia using 1.5–2.5% (v/v) isoflurane, ketoprofen (5 mg kg^{-1}), Ethiqa XR (3.25 mg kg^{-1}) and bupivacaine (1 mg kg^{-1}), and a 1-cm incision was made to expose the rib cage. Then, the ElHyX-based glucose sensor was adhered to the outer surface of rib cage. The incision was closed with 5–0 Prolene (for muscles) and 4–0 Nylon (for skin) sutures. The output end of the implanted ElHyX-based ECG sensor was connected to CHI760 for signal recording. Retro-orbital glucose (0.36 g kg^{-1}) injection was performed during the test.

To evaluate the performance of ElHyX-based nerve cuff, healthy rats were anaesthetized and administered analgesia using 1.5–2.5% (v/v) isoflurane, ketoprofen (5 mg kg^{-1}), Ethiqa XR (3.25 mg kg^{-1}) and bupivacaine (1 mg kg^{-1}), and a 2-cm incision was made to expose the sciatic nerve. Then, the ElHyX-based nerve cuff was adhered and wrapped around the nerve. The input end of the nerve cuff was connected to PowerLab equipped with stimulus isolator to apply electrical stimulation.

To evaluate the performance of the ElHyX-based closed-loop blood glucose regulation system, diabetic rats were anaesthetized and administered analgesia using 1.5–2.5% (v/v) isoflurane, ketoprofen (5 mg kg^{-1}), Ethiqa XR (3.25 mg kg^{-1}) and bupivacaine (1 mg kg^{-1}). The ECG sensing electrode and glucose sensing electrode were secured using the methods described above. To secure the vagus nerve cuff, a 2-cm incision was made along the midline of the neck to expose the vagus nerve. Then, the nerve cuff was adhered and wrapped around the nerve. In the case of selective eVNS, the nerve was sectioned proximal form the electrode. Unless otherwise specified, the input and output terminals of the system were connected to PowerLab (with stimulus isolator) and CHI760 for signal recording and VNS.

In vivo biocompatibility

Implantation studies were performed in accordance with a modified intradermal induction protocol based on US Food and Drug Administration guidelines and approved by the Institutional Animal Care and Use Committee at the California Institute of Technology (protocol no. IA23-1800). Twelve-week-old male healthy rats (Sprague-Dawley, Charles River Laboratories) were anaesthetized with 2.5% (v/v) isoflurane and administered analgesics, including Ethiqa XR (3.25 mg kg^{-1}), ketoprofen (5 mg kg^{-1}) and bupivacaine (1 mg kg^{-1}). A 1-cm incision was made on the dorsal skin of each animal to create a subcutaneous pocket, into which the test samples were implanted. After 28 days, animals were humanely euthanized, and main organs and the surrounding tissues were collected. The specimens were fixed in 4% paraformaldehyde at 4 °C overnight, followed by extensive washing with DPBS (five times) and incubation in 30% sucrose at 4 °C overnight. Samples were then embedded in optimal

cutting temperature compound (Thermo Fisher Scientific), flash frozen and cryosectioned into 50-µm sections. Sections were mounted onto microscope slides, paraffin-embedded and subjected to H&E staining. For deparaffinization, sections were immersed in xylene (two cycles of 10 min each), followed by 100% ethanol (two washes of 5 min each), then sequentially immersed in 95% and 70% ethanol for 1 min each, and finally rinsed with deionized water. Next, the sections were stained with filtered Harris haematoxylin for 10 s, followed by immersing in water to dilute the dye. The sections were then counterstained with eosin by submerging in eosin stain for ~30 s before water rinsing. Subsequently, sections were dehydrated in 100% ethanol (two cycles, 5 min each) and cleared in xylene (two cycles, 5 min each). Finally, sections were mounted using a resin-based mounting medium. For immunohistochemistry, sections were incubated with anti-CD3 [SP7] (ab16669) primary antibody, followed by Alexa Fluor 488-conjugated goat anti-rabbit IgG H&L secondary antibody. Macrophages were labelled using anti-CD68 [FA-11] (25-0681-82) directly conjugated to PE-Cyanine7 (Invitrogen). Nuclei were counterstained with 4′,6-diamidino-2-phenylindol. Slides were mounted using ProLong Diamond Antifade Mountant (Invitrogen) and imaged with a ZEISS LSM 800 confocal microscope.

Statistics and reproducibility

The experiments shown in Figs. 2b,j,k, 3b,c and 4j–l were independently repeated three times with similar results. Quantitative results are shown as mean ± standard deviation (s.d.). No statistical methods were used to predetermine sample sizes, but our sample sizes are similar to those reported in previous publications[47,48]. The data distribution was assumed to be normal, but this was not formally tested. No data were excluded from the analyses. Experimental animals were assigned randomly to experimental groups. Data collection and analysis were not performed blind to the conditions of the experiments.

Reporting summary

Further information on research design is available in the Nature Portfolio Reporting Summary linked to this article.

Data availability

The data supporting the results in this study are available within the Article and its Supplementary Information. Source data are provided with this paper.

References

45. Pandit, R. et al. Effect of epoxidation of diene component of SBS block copolymer on morphology and mechanical properties. *Macromol. Symp.* **315**, 152–159 (2012).
46. He, J. & Zhang, L. Chemical adhesion of a hydrogel on an elastomer surface enabling directionally-bendable actuators. *J. Mater. Chem. C* **10**, 2938–2944 (2022).
47. Tang, S. et al. Enzymatic microbubble robots. *Nat. Nanotechnol.* **21**, 397–406 (2026).
48. Wang, M. et al. Printable molecule-selective core–shell nanoparticles for wearable and implantable sensing. *Nat. Mater.* **24**, 589–598 (2025).

Acknowledgements

We acknowledge the critical support and infrastructure provided for this work by the Kavli Nanoscience Institute at Caltech.

Author contributions

J.L. and W.G. initiated the concept and designed the studies. J.L., K.F., X.M., C.W., J.M., Y.C., Y.S. and Y.X. performed materials preparation, characterization, validation and sample analysis. W.G. and J.L. cowrote the paper. All authors contributed to the data analysis and provided the feedback on the paper.

Funding

W.G. discloses support for the project of this work from National Institutes of Health grants R01DC021461 and R01HL155815, Army Research Office grant W911NF-23-1-0041, National Science Foundation grant 2145802, US Army Medical Research Acquisition Activity grant HT9425-24-1-0249, and Heritage Medical Research Institute.

Competing interests

The authors declare no competing interests.

Additional information

Supplementary information The online version contains supplementary material available at https://doi.org/10.1038/s41563-026-02624-4.

Correspondence and requests for materials should be addressed to Wei Gao.

Peer review information *Nature Materials* thanks Bozhi Tian, Hyunwoo Yuk and Sheng Xu for their contribution to the peer review of this work.

Reprints and permissions information is available at www.nature.com/reprints.

nature research

Corresponding author(s): Wei Gao

Last updated by author(s): Apr 25, 2026

Reporting Summary

Nature Research wishes to improve the reproducibility of the work that we publish. This form provides structure for consistency and transparency in reporting. For further information on Nature Research policies, see our Editorial Policies and the Editorial Policy Checklist.

Statistics

For all statistical analyses, confirm that the following items are present in the figure legend, table legend, main text, or Methods section.

n/a	Confirmed	
☐	☒	The exact sample size (*n*) for each experimental group/condition, given as a discrete number and unit of measurement
☐	☒	A statement on whether measurements were taken from distinct samples or whether the same sample was measured repeatedly
☒	☐	The statistical test(s) used AND whether they are one- or two-sided *Only common tests should be described solely by name; describe more complex techniques in the Methods section.*
☒	☐	A description of all covariates tested
☒	☐	A description of any assumptions or corrections, such as tests of normality and adjustment for multiple comparisons
☐	☒	A full description of the statistical parameters including central tendency (e.g. means) or other basic estimates (e.g. regression coefficient) AND variation (e.g. standard deviation) or associated estimates of uncertainty (e.g. confidence intervals)
☒	☐	For null hypothesis testing, the test statistic (e.g. *F*, *t*, *r*) with confidence intervals, effect sizes, degrees of freedom and *P* value noted *Give P values as exact values whenever suitable.*
☒	☐	For Bayesian analysis, information on the choice of priors and Markov chain Monte Carlo settings
☒	☐	For hierarchical and complex designs, identification of the appropriate level for tests and full reporting of outcomes
☐	☒	Estimates of effect sizes (e.g. Cohen's *d*, Pearson's *r*), indicating how they were calculated

Our web collection on statistics for biologists contains articles on many of the points above.

Software and code

Policy information about availability of computer code

Data collection	Presto blue staining (Invitrogen) was used for quantitative analysis of cell viability and Biotek plate reader was used for OD measurements. Zeiss confocal microscope was used for cell imaging. CH Instrument and PowerLab was used for sensor characterization.
Data analysis	Microsoft Excel 2021 and Origin 2021 were used to analyze all data, plot the data and calculate the statistical parameters.

For manuscripts utilizing custom algorithms or software that are central to the research but not yet described in published literature, software must be made available to editors and reviewers. We strongly encourage code deposition in a community repository (e.g. GitHub). See the Nature Research guidelines for submitting code & software for further information.

Data

Policy information about availability of data

All manuscripts must include a data availability statement. This statement should provide the following information, where applicable:

- Accession codes, unique identifiers, or web links for publicly available datasets
- A list of figures that have associated raw data
- A description of any restrictions on data availability

The data supporting the results in this study are available within the paper and its Supplementary Information. Source data are provided with this paper.

Field-specific reporting

Please select the one below that is the best fit for your research. If you are not sure, read the appropriate sections before making your selection.

☒ Life sciences ☐ Behavioural & social sciences ☐ Ecological, evolutionary & environmental sciences

For a reference copy of the document with all sections, see nature.com/documents/nr-reporting-summary-flat.pdf

Life sciences study design

All studies must disclose on these points even when the disclosure is negative.

Sample size	For in vitro cell studies at least 3 samples per group per time point was tested (n≥3). For rats studies 3 animals per condition was tested.
Data exclusions	No data exclusion.
Replication	All attempts at replication were successful when following the device fabrication process described in the paper.
Randomization	The device was fabricated with same process and was tested in all animals under same conditions. Randomization was therefore not relevant to the study.
Blinding	Not relevant, because a blinding process wouldn't influence the sampling result.

Reporting for specific materials, systems and methods

We require information from authors about some types of materials, experimental systems and methods used in many studies. Here, indicate whether each material, system or method listed is relevant to your study. If you are not sure if a list item applies to your research, read the appropriate section before selecting a response.

Materials & experimental systems

n/a	Involved in the study
☐	☒ Antibodies
☐	☒ Eukaryotic cell lines
☒	☐ Palaeontology and archaeology
☐	☒ Animals and other organisms
☐	☒ Human research participants
☒	☐ Clinical data
☒	☐ Dual use research of concern

Methods

n/a	Involved in the study
☒	☐ ChIP-seq
☒	☐ Flow cytometry
☒	☐ MRI-based neuroimaging

Antibodies

Antibodies used	anti-CD3 [SP7] (ab16669) and anti-CD68 (ab31630) from Abcam.
Validation	N/A

Eukaryotic cell lines

Policy information about cell lines

Cell line source(s)	Primary Dermal Fibroblast; Normal, Human, Adult (HDFa) (ATCC, cultured under 37 °C and 5% CO2)
Authentication	All cells were purchased from ATCC and have been ethically sourced and authenticated by thorough QC testing by ATCC.
Mycoplasma contamination	We did not observe any mycoplasma contamination in our cell cultures.
Commonly misidentified lines (See ICLAC register)	N/A

Animals and other organisms

Policy information about studies involving animals; ARRIVE guidelines recommended for reporting animal research

Laboratory animals	Zucker Diabetic Fatty (ZDF) rats (Charles River Laboratories, Wilmington, MA, USA) and Sprague Dawley (SD) rats (Charles River Laboratories, Wilmington, MA, USA)
Wild animals	N/A
Field-collected samples	N/A
Ethics oversight	The animal protocol was approved by the Institutional Animal Care and Use Committee (IACUC) at California Institute of Technology.

Note that full information on the approval of the study protocol must also be provided in the manuscript.

Human research participants

Policy information about studies involving human research participants

Population characteristics	Healthy individuals between the ages of 18 and 65.
Recruitment	The participating subjects were recruited from Caltech campus. There were no self-selection biases or other biases.
Ethics oversight	Institutional Review Board (IRB) at California Institute of Technology

Note that full information on the approval of the study protocol must also be provided in the manuscript.